Deployment-invariant probability of detection characterization for aerial LiDAR methane detection

Michael J. Thorpe[1,*], Aaron Kreitinger[1], Dominic T. Altamura[1], Cameron D. Dudiak[1], Bradley M. Conrad[2], David R. Tyner[2], Matthew R. Johnson[2], Jason K. Brasseur[1], Peter A. Roos[1], William M. Kunkel[1], Asa Carre-Burritt[1], Jerry Abate[1], Tyson Price[1], David Yaralian,[1] Brandon Kennedy[1], Edward Newton[3], Erik Rodriguez[3], Omar Ibrahim Elfar[3], Daniel J. Zimmerle[4]

[1] Bridger Photonics, Inc., Bozeman, MT, 59715, USA

[2] Energy & Emissions Research Laboratory, Department of Mechanical and Aerospace Engineering, Carleton University, Ottawa, ON, Canada, K1S 5B6

[3] Southern California Gas Company, Los Angeles, CA, 90660, USA

[4] The Energy Institute, Colorado State University, Fort Collins, CO, 80524, USA

*Correspondence: Michael Thorpe
Mike.Thorpe@bridgerphotonics.com

This paper has been submitted for peer reviewed publication to Remote Sensing of Environment

Abstract

Accurate detection sensitivity characterization of remote methane monitoring technologies is critical for designing, implementing, and auditing effective emissions monitoring and mitigation programs. Several research groups have developed test methods based on single/double-blind controlled release protocols and regression-based data analysis techniques to create probability of detection (PoD) models for characterizing remote sensor detection sensitivities. The previously created methods and models account for some of the important factors that affect detection sensitivity, such as wind speed, and in the case of Conrad et al. flight altitude. However, these models do not account for other important factors, such as terrain albedo, variation in individual sensor performance, or spatial density of the remote sensing measurements. In this paper, we build on the work of Conrad et al. by introducing a gas concentration noise (GCN) model for Gas Mapping LiDAR aerial methane detection technology that, when combined with wind speed at the emission location, accounts for all significant sensor and environmental parameters that affect detection sensitivity for scenarios involving an isolated emission source resulting in a single methane plume. We incorporate the GCN model into Conrad et al.'s PoD model and apply it to several sets of controlled release data acquired across widely varying deployment and environmental conditions to develop PoD models for Bridger Photonics Inc.'s first- and second-generation (GML 2.0) Gas Mapping LiDAR sensors. Finally, we compare controlled release data acquired by GML 2.0 in different geographic regions and terrain cover types, in different wind conditions, deployed on different aircraft types, and with different flight parameters. Results show that the GML 2.0 PoD model remains valid regardless of the location or conditions under which the sensors are deployed, and the aircraft and flight parameters used for deployment. Based on PoD measurements in 12 production basins across North America, the average 90% PoD emission rate for sites measured by GML 2.0 in 2023 was 1.27 kg/h.

Keywords: LiDAR, remote sensing, methane, emissions monitoring, detection sensitivity, probability of detection, gas mapping

1 Introduction

Reducing methane emissions to the atmosphere, especially from oil and gas infrastructure, is understood to be among the most cost-effective approaches available for mitigating the near-term effects of climate change.[1] However, recent efforts to quantify methane emissions, while subject to high levels of uncertainty, suggest that emissions remain stubbornly high.[2]dMany studies have measured elevated methane emissions for oil and gas production areas, using regional aircraft,[3,4] tower,[5] and satellite methods,[6] but these approaches cannot easily attribute emissions to individual operations and sources as required to guide emissions mitigation efforts. The need for source-resolved data has spurred extensive aerial measurement campaigns using technologies that can attribute emissions to individual equipment groups or equipment units. Total emissions estimates from source-resolved measurement efforts are subject to uncertainty due to the difficulty of monitoring the vast oil and gas infrastructure with sufficient detection sensitivity, sample size, frequency, and quantification accuracy to reliably inventory emissions. Recent efforts to evaluate the performance of existing monitoring technologies[7,8] and understand the distribution of emissions from oil and gas infrastructure[9,10] indicate that existing technologies can produce accurate emissions inventories (i.e. low-uncertainty) if monitoring campaigns are designed with sufficient detection sensitivity, sample size, monitoring frequency, quantification accuracy, and emission source resolution and attribution. Reliable, measurement-based emissions inventories are expected to form the basis for measurement, monitoring, reporting, and verification (MMRV) programs to benchmark emissions and track mitigations as companies and governments pursue their stated emissions reduction targets.[11] Emissions inventories with lower uncertainties will allow stakeholders to confidently resolve smaller changes in emissions behavior enabling operators to validate the efficacy of mitigation efforts, such as leak detection and repair (LDAR) programs and improvements to equipment designs, facility designs, and operational processes.

Characterizing the detection sensitivity of a monitoring technology is challenging because the probability of detecting (PoD) an emission source can vary strongly with many environmental conditions and, in the case of aerial technologies, with the flight parameters of the sensor deployment. Until recently, the detection sensitivity of remote monitoring technologies was generally characterized by the minimum detection limit (MDL), which defines the smallest emission rate observed by the monitoring technology. Recent testing of airborne sensors has shown that environmental parameters have a strong effect on the probability of detection for a given emissions source,[7,8,12] such that the emission rate corresponding to, for example, 90% PoD for a technology can be more than an order of magnitude greater than a cited MDL that may be derived from different deployment parameters or favorable environmental conditions.[13,14] Moreover, even for fixed operational and environmental conditions, the probability of detection has been shown to vary rapidly as a function of emission rate, such that a small change in emission rate can lead to drastic changes in the PoD for a particular emission source. These discrepancies between MDL and the true detection sensitivity of monitoring technologies have led to significant confusion in recent attempts to characterize emission rate distributions and intermittency of emission sources from oil and gas infrastructure.

More recent efforts to characterize detection sensitivity have used measurements of the wind speed near the controlled release location and a linear predictor logistic inverse link (LP-LIL) model to compute the PoD as a function of the wind speed normalized emission rate.[7, 12, 15] This method represented a significant improvement over MDL characterization by quantifying the dependence of emission rate PoD on wind speed. However, it provides limited flexibility in modeling the functional form of the wind speed dependence, assuming a linear relationship which results in unrealistically good detection sensitivity predictions for small emissions as wind speed approaches zero. It also provides no mechanism for modeling other parameters that affect PoD, such as flight altitude, flight speed, terrain albedo, and others. Bell et al. used the LP-LIL method to characterize the dependence of flight altitude by conducting controlled release (CR) tests at different flight altitudes and fitting separate LP-LIL models to the corresponding data sets.[7] This work showed the 90% PoD emission rate for a fixed wind speed increased by 65% when the flight altitude was increased by just 35%. Since the LP-LIL analysis lacks the ability to model flight altitude as a continuous variable it was not possible to determine the functional form of the PoD dependence on flight altitude using this analysis. Moreover, the other parameters that affect PoD were not considered, meaning the results are only valid for areas with similar conditions to the controlled release test site at the time the study was performed when they are scanned with equivalent sensor and flight parameters.

Conrad et al. improved upon the LP-LIL analysis by developing a method that allows generalized relationships between the emission rate and variables that affect PoD using a maximum likelihood fit method.[8] This approach provides a statistically robust method to compare the fit performance of various candidate models and to determine coefficient values that minimize information loss of the models relative to a set of controlled release data points. They applied this method to GML controlled release data and found strong dependence of PoD on flight altitude 'h' with an optimized functional form of $h^{-2.44}$, very close to the theoretically expected functional form of $h^{-2.5}$, due to the combined effects of diminishing light collection and reduced measurement spatial density with increasing flight altitude.

In this paper we present a noise model for aerial LiDAR methane concentration measurements that distills the myriad parameters that affect detection sensitivity into a single parameter called gas concentration noise. We then develop a generalized PoD model with three input variables - emission rate, wind speed, and gas concentration noise – that is demonstrated to remain valid across a wide range of environmental conditions, deployment configurations, and sensor performance. This provides users of GML data robust estimates of detection sensitivity for every flyover pass and potential emission source location within the scanned infrastructure. These improvements to detection sensitivity characterization are expected to benefit a wide variety of applications in methane emissions monitoring including 1) auditable compliance with the detection sensitivity requirements set forth in new US and Canadian methane emissions regulations; 2) the ability to reliably estimate the measured and unmeasured portions of the methane emission distribution from individual monitoring campaigns; 3) development of accurate measurement-based methane emissions inventories and emission factors; and 4) certification of differentiated gas through dependable methane loss rate measurements.

2 Methods

2.1 Data acquisition

Data from controlled release testing campaigns conducted in four locations across North America were analyzed to produce deployment invariant PoD models for GML sensor versions 1 and 2 (GML 1.0 and GML 2.0). Table 1 lists the details for each controlled release test with a row for each unique single-blind testing location including the GML sensor version, test date range, aircraft type, flight speed, flight altitude, controlled release height, ground cover type, and ground cover reflectivity at the LiDAR methane measurement wavelength of 1651 nm. Descriptions of the GML 1.0 sensor can be found elsewhere in the literature.[8,16] Specifications for the GML 2.0 sensor are similar to GML 1.0 except that GML 2.0 acquires LiDAR path-integrated methane concentration measurements at a 33% faster rate for denser spatial distribution of LiDAR measurements and, as concluded in this study, achieves approximately 35% improved detection sensitivity performance relative to GML 1.0 under equivalent conditions primarily due to improvements in the LiDAR transceiver efficiency and the detection electronics' noise properties.

GML was deployed for each controlled release test using the typical contracted flight service provider companies and aircraft types that are used for commercial deployment in each test region and industry segment. For example, the campaigns in Midland, TX, Bozeman, MT, and Wonowon, BC were deployed on Cessna 172 fixed wing aircraft using typical flight parameters for production sector monitoring scans. The campaign in Los Angeles, CA was deployed on a Bell 206 helicopter using typical flight parameters for distribution sector monitoring scans (see Table 1). The organization that administered the controlled release tests in each region is listed in Table 1 using the following abbreviations: Colorado State University (CSU), Southern California Gas Company (SoCalGas, SCG), Bridger Photonics (BP), and Carleton University (CU).

Table 1. Details of the controlled release experiments conducted for this work.

GML version	Testing org	General Location	Aircraft type	Terrain type/reflectivity	Test type	Test Dates	Flyover # [total, valid, missed]	Release height (m)	Flight altitude (m)	Flight speed (mph)
1.0	CSU	Midland, TX	Cessna 172	sage desert/0.28	single-blind	October 4-8, 2021	420,411,158	3.3	141-223	90-120
2.0	SCG	Los Angeles, CA	Bell 206	pavement/0.19	single-blind	July 25, 2022 – July 26, 2022	93,82,43	0.5	142-176	60-90
2.0	SCG	Los Angeles, CA	Bell 206	road mix/0.2	single-blind	August 5, 2022 – December 16, 2022	282,235,142	0.5	140-191	60-90
2.0	BP	Bozeman, MT	Cessna 172	prairie grass/(0.22-0.41) snow/(0.08-0.12)	single-blind	September 7, 2022 – August 31, 2023	284,242,45	1.85	130-226	90-120
2.0	BP	Bozeman, MT	Cessna 172	prairie grass/(0.27-0.45) snow/0.14	single-blind	February 10, 2023 – May 19, 2023	217,197,47	1.85	142-239	90-120
2.0	BP	Bozeman, MT	Cessna 172	prairie grass/0.38	single-blind	August 16, 2023	18,18,4	1.85	86-229	90-120
2.0	BP	Bozeman, MT	Cessna 172	prairie grass/(0.26-0.29)	single-blind	August 16, 2023 – November 15, 2023	234,233,56	1.85	125-236	90-120
2.0	CU	Wonowon, BC	Cessna 172	operational production pads - road mix and grass/(0.17-0.39)	single-blind and double-blind	September 11, 2023 – September 14, 2023	529,515,71	1.15-1.19	205-279	90-120

For all single-blind testing campaigns the release point and anemometer were positioned away from topography, structures, and foliage that might disturb local wind flow to ensure the gas flow speed at the controlled release location was well characterized by the anemometer measurements. The controlled release point was positioned at a height above ground level (AGL) corresponding to the typical height of methane emissions from infrastructure being scanned in that region and industry segment. For all experiments, the anemometer(s) were positioned at least 1.85 m above ground level to avoid measurement resolution and accuracy limitations. A minimum time delay between changes to the mass flow controller rate and the subsequent flyover passes was enforced to allow adequate time for the methane plume to develop at each flow rate. Since the release locations were typically positioned near the center of the GML scan swath, the plume length was required to be two-thirds of the swath width to ensure the entire length of the plume within the scan swath corresponded to the new steady-state release rate being issued by the mass flow controller. The time threshold was based on the wind speed at the plume height (u) and the scan swath width, which depended on flight altitude with both GML sensor versions having a 32° field of view (FOV) resulting in a flight altitude (h) dependent scan swath width $s = 2tan(FOV/2)h$. An example computation of the minimum plume development time is as follows: given a flight altitude of 700' (213 m) AGL and a wind speed of 1 m/s the minimum delay for adequate plume development is calculated by $\Delta t_{min} = 2s/3u = 82\ s$. A controlled release flyover experiment with these parameters will only be considered valid if the time between the emission rate change and the flyover pass is greater than or equal to 82 s. For the flyover measurements presented here, the minimum plume development time varied from 7.3 s to 367 s with an average value of 53 s.

The equipment and protocols used for the CSU controlled release test are described in Ref. [7]. For the tests administered by SoCalGas in Los Angeles, CA methane from compressed cylinders (distribution system gas, 93.7% methane fraction) was released through Alicat MCP-50SLPM-D mass flow controllers with rated accuracy of ±0.8% of reading and ±0.2% of full scale at a height of 0.5 m AGL. A Young model

81000 ultrasonic anemometer (resolution 0.01 m/s and 0.1°, accuracy ±1% ±0.05 m/s and ±2°) was positioned within 20 feet of the controlled release points at a height of 3 m AGL to record the local wind speed and direction. For the tests conducted in Bozeman, MT, administered by Bridger, methane from compressed cylinders (General Distributing, 93% methane fraction) was released through Alicat MCR-250SLPM-D/5M mass flow controllers with rated accuracy of ±0.8% of reading and ±0.2% of full scale at a height of 1.85 m above ground level. Two Young model 91500 ultrasonic anemometers (resolution 0.01 m/s and 0.1°, accuracy ±2% ±0.3 m/s (0-30 m/s) and ±2°) were positioned within 20 feet of the controlled release points at a height of 1.85 m above ground level to record the local wind speed and direction.

Controlled methane releases tests conducted in Wonowon, BC were administered by CU Energy and Emissions Research Lab from within active and inactive oil and gas facilities using similar equipment and protocols to those described in Ref. [8]. Experiments were completed over four-days during September 11-14, 2023, and included releases from 20 different oil and gas production sites in Northern British Columbia. The sites ranged in complexity from single wellheads to a large gas processing plant, providing a diversity of infield measurement conditions with varying ground cover and reflectivity, on-site infrastructure, wind conditions, and the potential for interaction with additional on-site sources. Release test sites were selected and grouped into five sets of four locations balancing elevation changes and site spacing to maximizing the number of measurement laps per test circuit while allowing sufficient time between laps (approximately 3 to 4 minutes) for the ground team to change the release rates and/or release locations. In total, seven test circuits were flown with the number of flight passes ranging from 11 to 19 in each circuit. At each site, methane from compressed gas cylinders (>99% purity) was released vertically at 1 or 2 distinct locations simultaneously from small (rates of ~0.1-2.9 kg/h) and large (rates of ~1.6-64 kg/h) calibrated Bronkhorst thermal mass flow controllers at heights between 1.15 m and 1.19 m AGL, respectively. A custom heated regulator and liquid-gas heat exchanger system was used to manage Joule-Thomson cooling effects. This ensured the gas temperature prior to entering the mass flow controllers was suitable to maintain each controller's rated accuracy. After each mass flow controller, methane passed through approximately 20 m of flexible tubing allowing the release point to be moved between laps. Finally, local wind speed at 3 m AGL was measured using an ultrasonic anemometer (Anemoment TriSonica mini) with a rated accuracy of ± 0.2 m/s over a range of 0-10 m/s.Release rate data, as well as local wind speed data were recorded using GPS-synchronized data loggers to ensure data could be subsequently time-matched with aerial detection data during post processing. Controlled releases with measured 3 m wind speeds less than 0.5 m/s were discarded from the analysis to avoid high relative anemometer error, which filtered 14 flyover passes from the analyzed data set.

Wind speed at the plume location was estimated by mapping the observed wind speed u, measured at the anemometer location and height above ground level, to the plume height above ground level using a logarithmic wind profile equation:

$$u(z_2) = u(z_1)\frac{ln((z_2-d)/z_0)}{ln((z_1-d)/z_0)},$$

where $u(z_1)$ is the wind speed measured by the anemometer, z_2 is the measured plume height, d = 0.066 m, and z_0 = 0.01 m. The emitter height is used as a proxy for the plume height to map wind speed from measured height to plume height in cases where the release height and anemometer height differ. During typical GML scans the plume height for detected releases is estimated using a technique that compares the LiDAR gas concentration measurements of the plume from multiple view angles described in Ref [17].

Prior to each controlled release test, the group administering the test created a matrix of controlled release rates to be issued during the test. The release rates were withheld from Bridger's data processing team until after the detection analysis for the test was completed and Bridger had issued reports to the administering organization. In the case of the CU controlled release tests, Bridger was not aware that two releases were happening simultaneously nor that the locations of small-scale releases were changing and therefore effectively double-blind. The matrix of controlled release rates for the CSU, SCG, and BP tests were designed to cover the probability of detection interval from <5% to >99% PoD. Bridger supplied each testing group with the best available PoD characterization prior to the test to define the emission rate intervals based on the flight parameters used for each test and the environmental conditions observed during the test. For all tests, Bridger deployed GML flyovers of the test site before the test to determine the terrain reflectivity near the release location. Terrain reflectivity was estimated from GML measurements using the LiDAR equations presented in Supplemental Material S1. For the tests administered by CSU, SCG, and BP, release rate intervals were defined for wind speed intervals 0-5 mph, 5-10 mph, and 10-20 mph to account for the wind speed dependence on the detection probability. Additional sets of emission rates for the three wind speed intervals were defined for different flight altitudes for the CSU and BP tests. The SCG tests were limited to a single altitude. For the Wonowon, BC test, administered by CU, flights were nominally conducted at a single flight altitude, although hilly topography led to significant variation in the actual altitude of individual flyover passes. Release rates for the CU test were selected to ensure good sample coverage near the nominal detection limit of the instrument. This was accomplished by inverting Bridger's preliminary PoD model for GML 2.0 and evaluating the emission rate corresponding to a random PoD between 0.5% and 99.5% given local, anemometer-measured, average wind speed during the preceding minute and a random GCN between 18 and 28 ppm-m (based on preliminary LiDAR measurements). Controlled releases spanned 0.13–64.3 kg/h, with 19 additional zero releases performed to evaluate the frequency of false positives of which there were none.

2.2 Data processing

Data acquired during GML controlled release tests were processed using Bridger's standard work practice. First, the raw sensor data is processed using an automated routine to determine the locations and extents of regions of elevated methane concentration (i.e., methane plumes, also referred to as detections) relative to ambient methane concentration levels, using the statistical algorithm described in Ref. [18]. Automated detection processing used the same algorithm and calibration parameters as commercial GML scans, thereby eliminating the possibility of human bias or subjectivity in the identification of detection events. After the automated processing step, Bridger's data processors use a custom software application to assign emission source locations to the methane detection plume images. First, the underlying topographic LiDAR point cloud data, colored by the signal-to-noise ratio of the path-integrated gas concentration for each LiDAR measurement point is analyzed to determine if a source location can be assigned. The threshold for assigning an emitter to a detected methane plume is three or more adjacent LiDAR points with path-integrated gas concentration signal-to-noise ratio exceeding a fixed threshold that is identical to the threshold used for commercial operations. Assigned emission locations within 5 m of the controlled release location are marked as *detections* and flyover passes without corresponding emission locations are marked as *misses*. Next, the plume height is determined for detections as described previously. The detections and misses along with flyover timestamp, source location, and wind speed at the measured plume height are compiled into a report that is issued to the testing organization and used for subsequent PoD analysis.

2.3 Gas concentration noise model

Gas Mapping LiDAR uses wavelength modulation spectroscopy to perform path-integrated methane concentration measurements along the path traversed by the transmitted LiDAR beam between the airborne sensor and the remote topographic target that backscatters the LiDAR beam. Lock-in detection is performed on the received LiDAR signal at harmonics of the modulation frequency, similar to Ref [19]. A mathematical description of the LiDAR equations for the first three harmonic components of the received signal is presented in Supplementary Material S1. The path-integrated methane concentration (C_{PI}) for each LiDAR measurement is calculated by:

$$C_{PI} = \frac{mP_{2f}}{2P_{1f}}\, \gamma \left(T, p, \frac{mP_{2f}}{P_{1f}}, \eta, \xi\right),$$

where:

P_{1f}	=	first harmonic of the received optical power
P_{2f}	=	second harmonic of the received optical power
m	=	the intensity modulation depth that relates P_{1f} to the total average received laser power
γ	=	coefficient that relates the ratio $\frac{mP_{2f}}{2P_{1f}}$ to the path-integrated concentration
η	=	laser modulation parameters of the transmitted LiDAR beam
ξ	=	methane spectroscopic parameters
T	=	atmospheric temperature
p	=	atmospheric pressure

A gas concentration noise (GCN) value can be computed for each LiDAR measurement using a calibrated noise model. The GCN model includes contributions from incoherent noise sources (n_{in}) and coherent noise sources (n_{cn}) and has the following functional form:

$$GCN = \sqrt{n_{in}^2 + n_{cn}^2},$$

where n_{in} includes shot noise, Johnson noise, and relative intensity noise and n_{cn} includes speckle noise[20,21]. The equation used to calculate the incoherent noise contribution to each LiDAR measurement is:

$$n_{in} = \frac{m\gamma NEP}{2P_{1f}\sqrt{\Delta t}},$$

where:

NEP = noise equivalent power without considering coherent noise, and

Δt = LiDAR gas concentration measurement duration.

A mathematical description of NEP is presented in Supplementary Material S2. The detection system NEP and the LiDAR transmitter/receiver speckle noise (n_{cn}) are calibrated during sensor manufacturing and validated through flight testing. Flight test validation is performed by computing the observed gas concentration noise using statistical analysis of sets of measured LiDAR gas concentration values and comparing them against the GCN values produced for each individual LiDAR gas concentration measurement by the model. A description of the calibration process, with example flight test data is presented in Supplementary Material S3. To account for detection sensitivity effects related to the spatial distribution and density of individual LiDAR measurements, and to create gas plume imagery, the geo-registered gas concentration and GCN values are averaged onto a raster grid with 2 m pixel size using the weighted average described in Supplementary Material S4. Due to the near conical scan pattern of GML LiDAR measurements, there is significant variation in spatial density of gas concentration measurements as a function of position across the GML scan swath, with the center of the scan swath having the lowest spatial density, and the highest density near the edges. Since the majority of flyover passes presented in this work targeted the controlled release locations near the center of the scan swath, the associated GCN values represent the worst possible detection sensitivity when compared to otherwise equivalent test conditions with emission sources positioned randomly within the GML scan swath.

2.4 Probability of detection model

The emission rate probability of detection model is adapted from Ref [8] to use raster pixel gas concentration noise with local wind speed and the emission rate issued during the controlled release test. Similar to Ref [8], PoD is modeled using the Bernoulli distribution with a 'predictor' function g(x;β) with coefficients β and variables x = [u, n, Q], where u, n, and Q represent wind speed, (raster pixel GCN)/1000, and emission rate, respectively. The model relates the predictor function to PoD using an 'inverse link' function F(g(x;β);α) with coefficients α, such that the probability of GML detecting an emission x with rate Q at a location with wind speed u, and $n = (raster\ pixel\ GCN)/1000$ is given by,

$$POD \stackrel{\text{def}}{=} \mathrm{F}(\mathrm{g}(\mathrm{x};\beta);\alpha).$$

Values of the inverse link coefficients α are held constant such that the mean and variance for the corresponding inverse link function probability distributions are equal to one. Maximum likelihood estimation (MLE) is used to optimize the coefficient values for candidate pairs of predictor and inverse link functions by minimizing the negative logarithm of the likelihood function (NLLF) for the Bernoulli distribution. The Akaike Information Criterion (AIC) is used to compare the MLE optimization outcomes for various functional forms to determine the predictor and inverse link functions that best represent the controlled release data while penalizing excessive model coefficients.[22] To arrive at the best PoD model we tested the predictor and inverse link functions described in Ref [8] and shown in Supplementary Material S5 Table 2.

3 Results

3.1 GML 1.0

The single-blind controlled release test administered by CSU in Midland, TX in early October 2021 represents the most comprehensive data set for characterizing GML 1.0 detection sensitivity. The test consisted of 420 flyover passes with emission rates below 4 kg/h, 411 of which met the criteria for a valid experiment (e.g., emission location within LiDAR swath coverage, mass flow controller and anemometer equipment functioning properly, and adequate plume development time before flyover pass). Of the 411 valid flyover passes, 253 of the releases were detected and 158 were missed, as shown in Table 1. Histograms of the test conditions including emission rates, wind speeds, and raster pixel GCN values for each flyover pass are shown in Figure 1 a-c. Wind speed conditions during the test varied between 0.4 m/s and 6.4 m/s with an average speed of 3.36 m/s. Raster pixel GCN values ranged from 13.1 ppm-m to 46.5 ppm-m and had two distinct peaks at 17 ppm-m and 27 ppm-m corresponding to the two flight altitudes targeted during the test, 500' (152 m) and 675' (206 m) AGL, respectively. The detection data and optimized PoD model based on the MLE fits and AIC comparison are shown in Figure 1 d-e with blue circles indicating detections and red x's indicating misses. Figure 1 d) shows results for the 500' (152 m) AGL flyover passes. Slices of the optimized PoD model for 10%, 50%, and 90% PoD at a raster pixel GCN of 17 ppm-m are plotted in black with detection data for the raster pixel GCN interval 12-22 ppm-m. Similarly, Figure 1 e) shows results for the 675' (206 m) AGL flyover passes. Data is shown for the raster pixel GCN interval 22-32 ppm-m and slices of the optimized PoD model for 10%, 50%, and 90% PoD at a raster pixel GCN of 27 ppm-m are plotted in black. For each candidate model, the relative likelihood of minimizing information loss is shown in Supplementary Material S5 and the top two performing models are highlighted in green and yellow, respectively. The optimized PoD model for this controlled release data set consisted of the p4 predictor function and the Log Normal inverse link function with coefficient values listed in Supplementary Material S5, Table 3.

The optimized PoD model can be used to estimate the average detection sensitivity for GML 1.0 facility flyover passes in the Permian basin. Bridger does not have a pre-computed record of raster pixel GCN for GML 1.0 flights because that information was not integrated into the GML data platform until near the end of GML 1.0 commercial deployments. However, if we assume the controlled release test location is representative of terrain albedo in the greater Permian Basin, and that the average wind speed in Midland, TX, at the average emitter height as measured by GML (4.7 m) is 3.3 m/s, the optimized PoD model indicates the basin average 90% PoD emission rates for GML 1.0 at 500' (152 m) and 675' (206 m) AGL flight altitudes are 1.03 kg/h and 1.60 kg/h, respectively.

The lines for 10%, 50%, and 90% PoD based on the LP-LIL model developed in Ref [7] are plotted in gray in Figure 1 d-e for comparison. A visual inspection of the detection data with the two PoD models reveals noticeable discrepancies between the LP-LIL PoD predictions and the flyover data in several portions of the wind speed and raster pixel GCN parameter space. Compared to the generalized PoD model presented here, the LP-LIL model, which is based on wind-speed-normalized emission rates, tends to overestimate the detection sensitivity of the GML measurements, especially at low wind speeds. Specifically, the 90% PoD detection sensitivity estimated by the LP-LIL model is 50% lower than the generalized model at 1 m/s and 30% lower at 3 m/s wind speed, respectively.

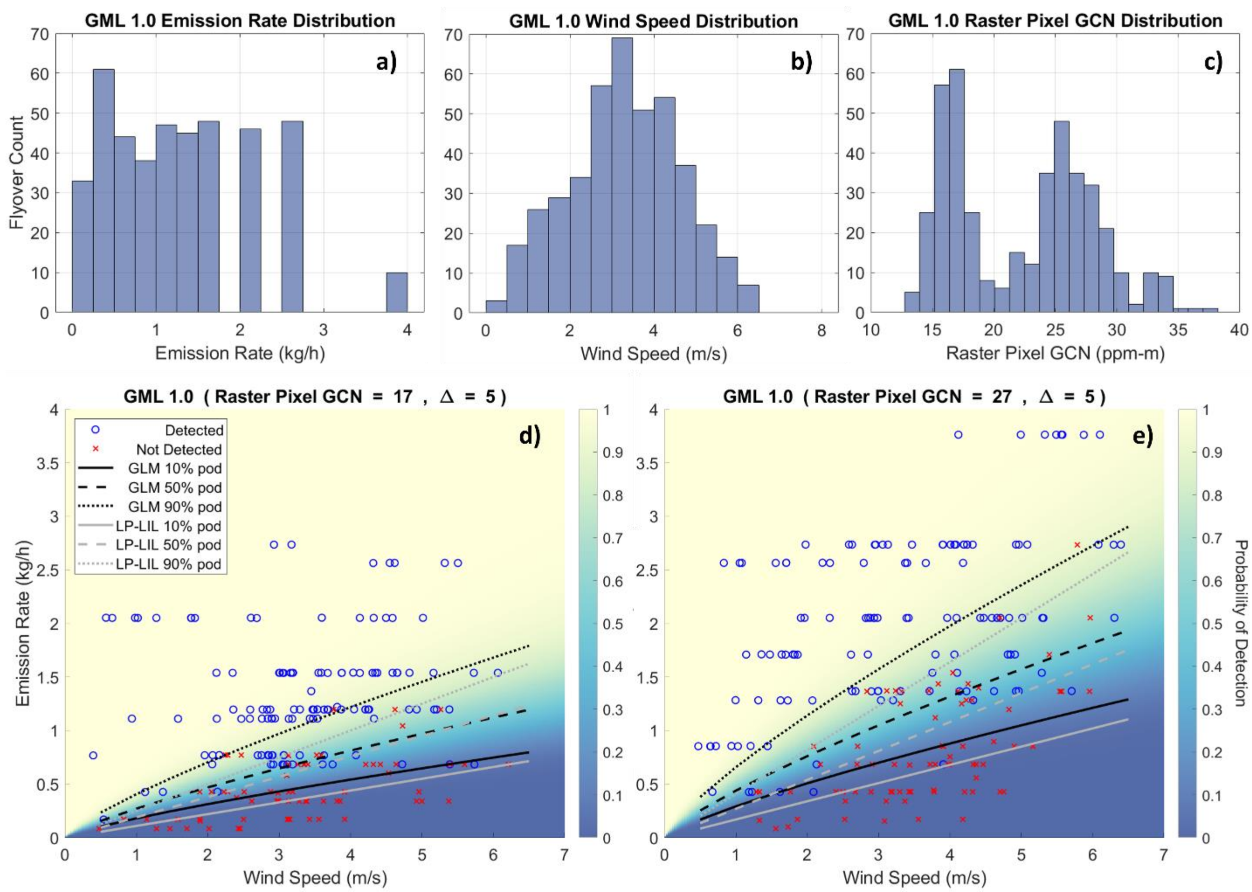

Figure 1. GML 1.0 controlled release data and PoD model results. The top row shows histograms for a) emissions rates, b) wind speeds, and c) raster pixel GCNs for the detection sensitivity portion of the controlled release test. Detection results corresponding to 500' AGL flyover passes d) and 675' AGL flyover passes e) are shown with blue circles indicating detections and red x's indicating misses. The presented detection data is filtered by raster pixel GCN intervals 12-22 ppm-m d) and 22-32 ppm-m e) and slices of the optimized PoD model for 10%, 50%, and 90% PoD are plotted in black for a raster pixel GCN of 17 ppm-m d) and 27 ppm-m e). PoD lines for the 500' and 675' AGL flyover passes for 10%, 50%, and 90% PoD based on the LP-LIL model developed in Ref. 7 are plotted in gray for comparison.

3.1.1 GML 2.0

Characterization of GML 2.0 PoD is based on three separate single-blind controlled release test campaigns. The first was administered by SoCalGas at two locations in the Los Angeles basin (LA) starting on July 25, 2022, and ending on December 16, 2022. The second test campaign was administered by Bridger Photonics' GML fleet management team at four locations near Bozeman, MT (BZN) and took place between September 7, 2022, and November 15, 2023. The third test was administered by Carleton University's (CU) Energy and Emissions Research Laboratory on 20 oil and gas production facilities near Wonowon, BC and took place between September 11, 2023, and September 14, 2023. The LA test consisted of 375 total flyover passes, 317 of which met the criteria for a valid experiment. Of the 317 valid flyover passes 132 of the releases were detected and 185 were missed. The BZN test consisted of 753 total flyover passes, of which 690 were valid, 538 were detected, and 152 were missed. The CU test consisted of 529 total flyover passes, of which 515 were valid, 444 were detected, and 71 were missed. Histograms of the test conditions including emission rates, wind speeds, and raster pixel GCN values are shown in Figure 3 a-d with the blue bars representing the LA test, mint representing BZN, and yellow representing BC. Wind speed conditions during the LA test varied between 0.5 m/s and 4.5 m/s with an average speed of 2.4 m/s. Raster pixel GCN values ranged from 6.0 ppm-m to 19.8 ppm-m with a single peak near the distribution mean of 12.1 ppm-m, corresponding to an average flyover altitude of 518' (158 m). Wind speed for the BZN test varied between 0.5 m/s and 9.7 m/s with an average speed of 2.9 m/s. Raster pixel GCN values ranged from 7.6 ppm-m to 54.5 ppm-m with two distinct peaks at 13 ppm-m and 19 ppm-m corresponding to the two flight altitudes targeted during the test, 500' (152 m) and 700' (213 m), respectively. Wind speed for the BC test with varied between 0.6 m/s and 7.6 m/s with an average speed of 2.3 m/s. Raster pixel GCN values ranged from 14.2 ppm-m to 33.4 ppm-m with a single peak near the distribution mean of 23.1 ppm-m, corresponding to an average flyover altitude of 722' (220 m).

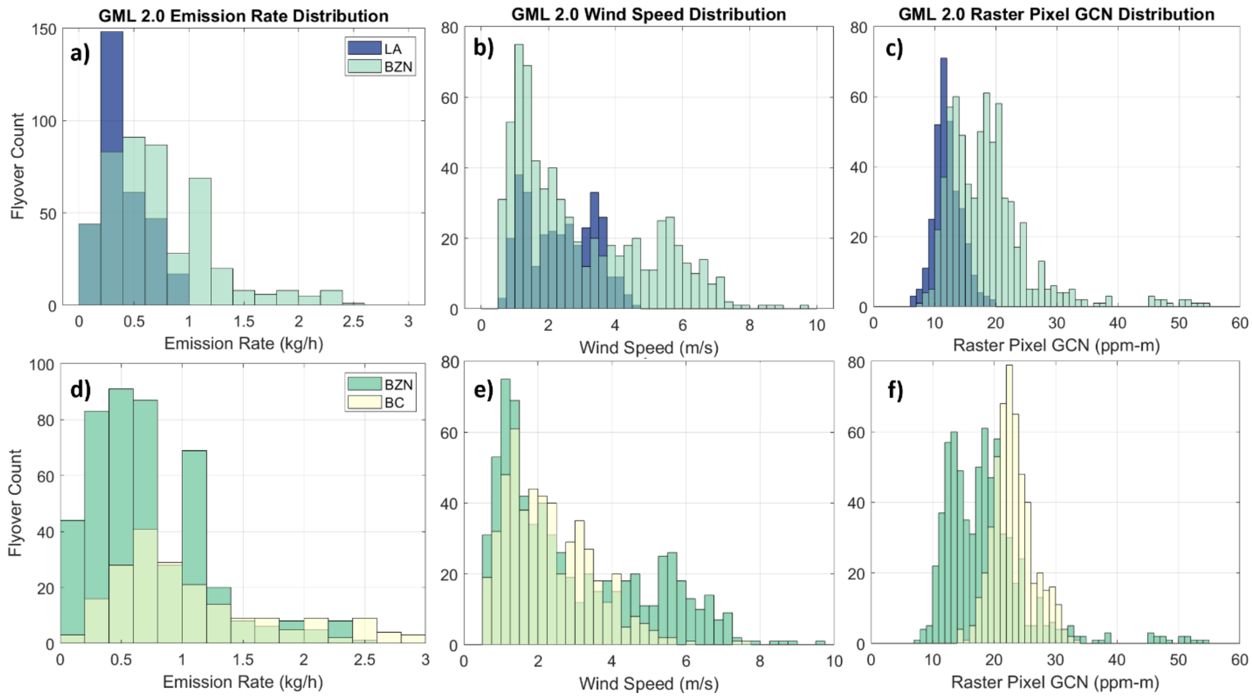

Figure 2. GML 2.0 PoD model results for controlled release test performed in Los Angeles, CA, Bozeman, MT, and Wonowon, BC. Histograms show the emissions rates a) & d), wind speeds b) & e), and raster pixel GCNs c) & f) issued for each flyover pass for the detection sensitivity portion of the test.

Detection data and optimized PoD models for each controlled release test region are shown in Figure 4 a)-d). Results for individual flyover tests are plotted with blue circles indicating detections and red x's indicating misses. All figures show black lines representing slices of the region-specific optimized PoD models for 10%, 50%, and 90% PoD. Figure 3 a) & b) show the LA and BZN data for the raster pixel GCN interval of 8-18 ppm-m and model slices computed at raster pixel GCN = 13 ppm-m, corresponding to the value of maximum raster pixel GCN overlap between the LA and BZN data sets. Figure 3 c) & d) show the BC and BZN data for the raster pixel GCN interval of 18-28 ppm-m and model slices computed at raster pixel GCN = 23 ppm-m, corresponding to the value of maximum raster pixel GCN overlap between the BC and BZN data sets. For the BC data set, only flyover passes corresponding to emission rates below 3.5 kg/h are plotted in Figure 3 c) to allow clear visualization of the optimized PoD curves. The complete data set is shown in Supplementary Material S6, Figure 9.

The performance of the candidate models for each data set and the functional form and coefficient values for the optimal models are shown in Supplementary Material S5, Table 3. The optimized PoD model for the LA data set consists of the p2 predictor function and the Burr inverse link function. The second-best performing predictor model was p3 with the Burr inverse link function, which had a 0.9512 probability of minimizing information loss relative to the optimal model. The small difference in performance between the p2 and p3 indicates weak preference for the p2 model, which exhibits a positive second derivative of the emission rate versus wind speed for surfaces of constant PoD. This is

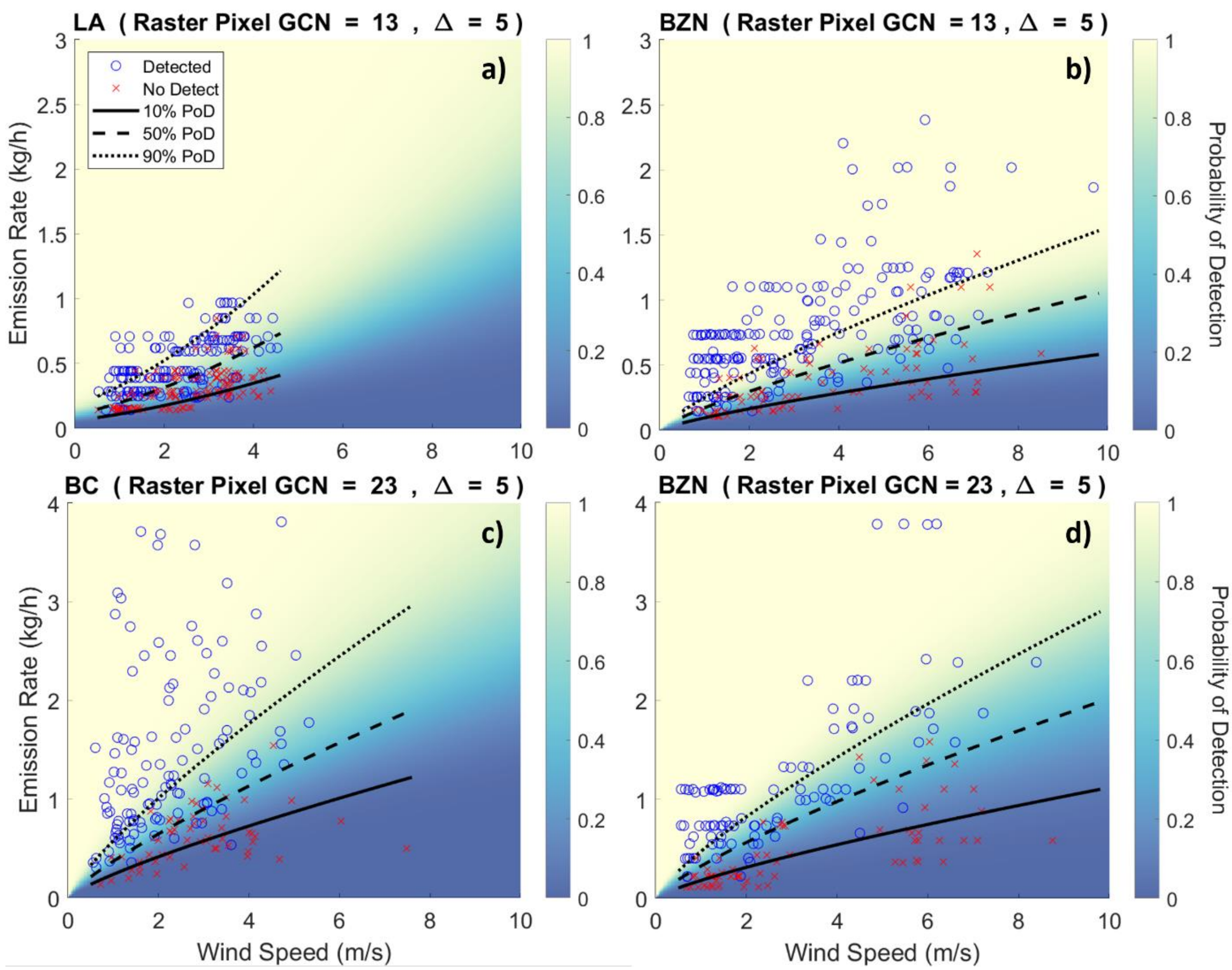

Figure 3. Detection results for GML 2.0 controlled release tests in the three regions – a) LA , b) & d) BZN, and c) BC. Flyover passes with blue circles indicate detections and red x's indicate misses. a) & b) show data for raster pixel GCN interval 8-18 ppm-m and c) & d) show data for raster pixel GCN interval 18-28 ppm-m. All figures show the optimized PoD model for 10%, 50%, and 90% PoD plotted in black at a raster pixel GCN of 13 ppm-m [a) & b)] and 23 ppm-m [c) & d)].

likely due to the limited range of wind speed conditions sampled in the LA controlled release tests. The optimized PoD model for the BZN data set consists of the p4 predictor function and the Weibull inverse link function. The GML 2.0 BZN data set has a significant preference for the p4 model, likely due to the larger range of wind speed and raster pixel GCN conditions sampled in the BZN controlled release tests. The optimized PoD model for the BC data set also consists of the p4 predictor function and the Log Normal inverse link function.

The optimized PoD model for the combination of GML 2.0 controlled release data sets acquired in LA, BZN, and BC are shown in Figure 4 for the low a) and high b) modes of the raster pixel GCN range. The optimized PoD model for the combined data set consists of the p4 predictor function and the Burr inverse link function. Preference for the p4 predictor function in the combined data set is likely due to the larger range of wind speed and raster pixel GCN conditions sampled in the BZN and BC controlled release tests that suppresses the super-linear trend of the p2 model at high wind speeds seen in the LA model.

Supplementary Material S5, Figure 8 a) and b) show the combined model plotted with the optimized PoD models for the LA, BZN, and BC data sets. Figure 8 c) and d) show the fractional difference between the combined GML 2.0 PoD model and the individual LA, BZN, and BC PoD models. Agreement within 30% fractional difference is observed between the individual and combined PoD models for both raster pixel GCN slices, all PoD thresholds, and for most of the wind speed range. The slightly better detection sensitivity performance for the BZN tests may be attributed to a combination of hardware improvements that reduced the noise for GML 2.0 sensors constructed after sensors were deployed for the LA and BC measurement campaigns and a transition to slightly more conservative selection of n_{in} and n_{cn} values from flight test data during calibration.

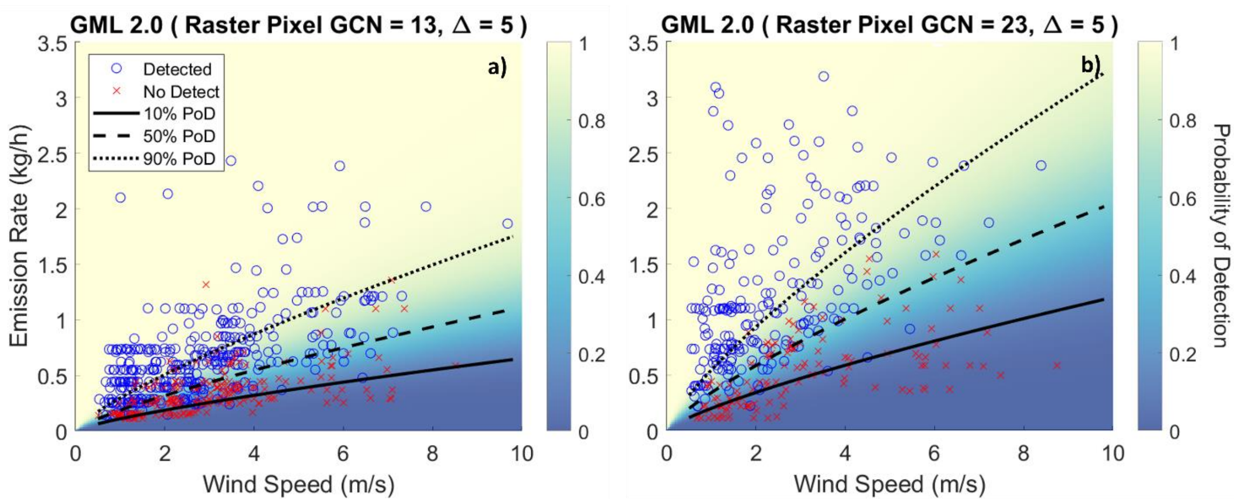

Figure 4. GML 2.0 PoD model from combination of LA, BZN, and BC data sets. a) Detection data and model results for the low end of the raster pixel GCN spectrum with data interval 8-18 ppm-m and model raster pixel GCN = 13 ppm-m. Detection data and model results for the high end of the raster pixel GCN spectrum with data interval 18-28 ppm-m and model raster pixel GCN = 23 ppm-m.

For GML 2.0 sensors, the raster pixel GCN values are computed as a standard output during automated data processing such that the optimized PoD models can be used to estimate the detection sensitivity for any GML scan data. For example, facility-level detection sensitivity estimates can be determined by inputting the average raster pixel GCN across the facility and the wind speed at the average emission source height above ground level into the model. Figure 5 shows facility-level detection sensitivity estimates for 2023 GML 2.0 scans in several regions across North America using the combined PoD model. Figure 5 a)-d) show histograms of 90% PoD facility-level detection sensitivity distributions for site scans in four oil and gas production regions. Figure 5 (right) shows a table containing the mean, median, and interquartile range for sites in 12 production regions and the Southern California Gas Company distribution infrastructure based on the 90% PoD detection sensitivity distributions. The best production sector facility-level detection sensitivity performance was achieved in the San Joaquin Valley (0.35 kg/h @ 90% Pod) where the GML sensor was deployed on a helicopter flying at 500' AGL and 70 mph, and the average wind speed at the average emission source height (2.3 m) was 1.7 m/s. The poorest upstream facility-level detection sensitivity performance was in Saskatchewan (1.804 kg/h @ 90% PoD) where GML was deployed on a fixed wing aircraft flying at 750' AGL and 100 mph and the average wind speed at the average emission source height (5.6 m) was 3.8 m/s. Since raster pixel GCN data is available for all areas

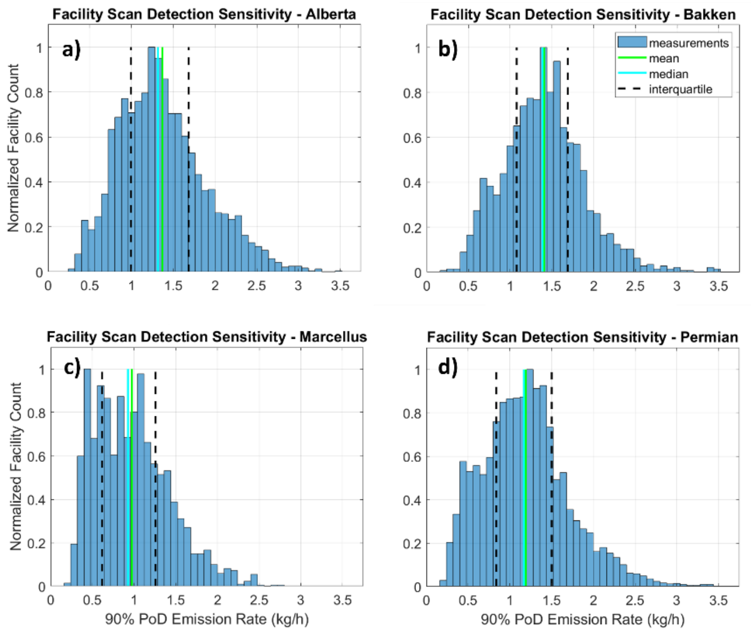

Basin	Mean	Median	Interquartile
Alberta	1.370	1.315	[0.993,1.684]
Anadarko	1.713	1.588	[1.233,2.183]
Bakken	1.407	1.389	[1.078,1.692]
British Columbia	1.326	1.323	[0.986,1.636]
Denver Julesburg	0.982	0.819	[0.670,1.547]
Eagle Ford	1.586	1.553	[1.337,1.809]
Haynesville	1.540	1.602	[1.326,1.957]
Los Angeles	0.339†, 0.524‡, 0.669††	N/A	N/A
Marcellus	0.974	0.927	[0.617,1.257]
Permian	1.191	1.168	[0.838,1.502]
San Joaquin Valley	0.353	0.353	[0.261,0.433]
Saskatchewan	1.804	1.772	[1.443,2.139]
Uinta	0.985	0.964	[0.856,1.106]

Emission source height above ground level: 0.2m - ground leaks†, 1.0m - meter leaks‡, 5.0m - roof top leaks††

Figure 5. (Left) Histograms of the facility-level detection sensitivity for 2023 scans in select regions. Histograms are normalized to the bin with maximum counts and are plotted with the distribution mean, median, and interquartile. (Right) Detection sensitivity statistics (mean, median, and interquartile) for 2023 GML scans in basins/provinces across North America.

covered by a GML scan, the detection sensitivity estimates can be computed for any region of interest. For example, emission source height information, obtained from monitoring data and/or infrastructure dimensional data, can be used in conjunction with raster pixel GCN and local wind speed data to compute facility- and equipment-level PoD estimates.

4 Discussion

The generalized PoD model presented in this work provides a practical method to generate localized detection sensitivity estimates for aerial LiDAR methane monitoring scans in scenarios involving geospatially isolated methane emission sources in relatively simple topography, structures, and foliage, typical of the production and transmission sectors of the natural gas supply chain. The model achieves this by distilling many significant factors affecting detection sensitivity into three measurable input variables, wind speed, gas concentration noise, and emission rate. The GCN consists of two physical sensing parameters, calibrated through flight testing, that enable the computation of a concentration noise value for each LiDAR path-integrated gas concentration measurement. Sets of scattered LiDAR concentration measurements are averaged onto a raster grid to provide a common spatial scale for comparing GCN values in different locations. Using a moderate number of controlled release experiments, covering a broad range of measurement conditions, the detection sensitivity performance of GML scans has been characterized in a several geographic regions and a wide variety of weather conditions, terrain albedo, and deployment configurations. Good agreement is observed between the derived PoD model and measurement results in these varied measurement conditions.

The optimized PoD model provides an auditable record of detection sensitivity performance with applications for several tasks in remote methane emissions monitoring. Examples include documenting and validating detection sensitivity performance for regulatory compliance scans, such as the EPA new source performance standards (e.g under OOOOb), and leveraging the PoD for detections, facility scans, and equipment scans to estimate the number and size of emissions that were present during GML scans but were unmeasured due to the statistical nature of emissions detection. The latter application will be critical for developing accurate methane emissions inventories and emissions intensities for tracking and informing emissions mitigations efforts and strategies.[9]

Pathways exist to further improve detection sensitivity estimates using higher accuracy and specificity wind speed and raster pixel GCN inputs that better match the actual conditions in the immediate vicinity of a methane emission source. For example, the accuracy of raster pixel GCN estimates will improve as the analysis area becomes more localized due to reduced likelihood of variations in terrain albedo, received optical power for LiDAR measurements, and LiDAR spatial point density within the analysis region. Accurate raster pixel GCN estimates will require maintaining a valid calibration of the GCN model for each deployed sensor, which can be accomplished through routine analysis of the scan data using the GCN model fit method described in Supplementary Material S3. While the facility-level detection sensitivity estimates shown in Figure 5, leveraging remote wind model data, represent a significant advancement in detection sensitivity characterization for aerial methane monitoring, the method will also become more accurate with high temporal resolution local wind speed information, such as anemometer measurements derived from local meteorological stations. Implementation of better wind measurement networks will benefit all types of methane emissions monitoring technologies. Finally, even more precise knowledge of the emission source height, which can be obtained from operator feedback from leak response activities, will enable better mapping of the observed wind speed to the wind speed at the emission source location.

Further testing will be required to characterize the detection sensitivity performance for scans of complex upstream oil and gas production sites, due to effects such as 1) spatially overlapping plumes from multiple, closely-spaced emission sources, 2) occlusion of the LiDAR measurement beam from the emission source location by facility equipment, 3) large and high-spatial-frequency variations in albedo near emission source locations, and/or 4) complex local wind fields that may deviate from local anemometer measurements. Additional opportunities to extend the scope of detection sensitivity characterization include spatially extended or distributed emission sources and scenes with large structures, complicated topography, and/or large and dense foliage. PoD characterization of complex measurement scenarios will benefit from analysis of topographic LiDAR data to determine portions of the measurement scene that are occluded for a given scan and to enable better wind speed estimates through fluid dynamics modeling. Characterization will also be necessary to create reliable PoD estimates for elevated temperature exhaust gas such as lit flares and compressor exhaust emissions. The current PoD model assumes all methane plumes are at ambient temperature. However, since the optical absorption of methane at 1651 nm decreases with increasing gas temperature, it is anticipated that there will be a detection sensitivity dependence on gas temperature, which is not captured in the formalism presented here. While GML routinely detects and quantifies hot emission sources, further research and characterization of a method to account for high-temperature gas (e.g. exhaust plumes) is warranted to ensure accurate PoD estimates for these emission sources.

Finally, the approach presented here provides a template for detection sensitivity analysis of remote methane emissions monitoring data which can be generally applied to any emissions detection solution. Specifically, the proposed method (a) characterizes the practical response of the solution's sensor system, using internally accessible estimates of noise or other factors, (b) combines sensor performance with key situational variables such as wind speed and emission rate, and (c) deploys a robust statistical model for probability of detection. Development of similar models for multiple methods would improve confidence in, and acceptance of, advanced emissions detection solutions for regulatory and voluntary reporting programs.

Acknowledgements

Bridger Photonics, Inc. thanks ARPA-E and the Montana Board of Research and Commercialization Technology for support in developing the Gas Mapping LiDAR hardware.

Funding Statement

Funding for this work came from various sources. The BP controlled release tests, data processing, data analysis, model development, software development, and manuscript preparation was supported by Bridger Photonics internal research and development funding. Funding for the controlled release tests performed by CU was provided by the British Columbia Government (grant #: RE23CASCG0004MY) and Natural Sciences and Engineering Research Council of Canada (NSERC, grant #: 06632). The work conducted by SoCalGas was funded through the California Public Utilities Commission and California Rate Payers under the auspices of Senate Bill SB 1371 and the CPUC Methane Leak Proceeding R.15-01-008. CSU release testing, subsequent analysis, and publication was funded by a grant from *The Environmental Partnership* and gas metering equipment provided by Bridger Photonics.

Author Contributions

MT: detection algorithm and gas concentration noise model development, extension of pod model to include gas concentration noise, controlled release experiment design, software, data analysis, visualization, writing – manuscript development, review, and editing, **AK**: detection algorithm and gas concentration noise model development, software, **DA, CD**: data curation, data analysis, software, visualization, writing – review, and editing **BC, DT, MJ**: pod model development, controlled release experiment design, data analysis, writing – review and editing, **JB**: gas concentration noise model calibration method development, writing – review and editing, **PR**, **WK, ACB, DZ**: writing – review and editing, **JA, TP**: software, **DY, BK**: data processing, writing – review and editing, **EN, ER, OIE**: single-blind controlled release experiment design and independent execution, data analysis, writing – review and editing.

Conflict of Interest

Bridger Photonics, Inc. profits from sales of Gas Mapping LiDAR methane emissions monitoring services.

Supplementary Material

S1 – Wavelength modulation spectroscopy LiDAR equations

The LiDAR equations describing the signal power in the first three harmonics of the signal received by the sensor are calculated as follows:

$$P_{DC} = \frac{A\chi\rho}{R^2} S_{DC} \,,$$

$$P_{1f} = \frac{A\chi\rho}{R^2} S_{DC} m \,,$$

$$P_{2f} = \frac{A\chi\rho}{R^2} S_{DC} \frac{2C_{PI}}{\gamma} \,.$$

Where:

S_{DC} = DC component of the LiDAR beam transmitted power,

P_{DC} = DC component of the LiDAR received power,

A = area of the receiver,

χ = receiver optics collection efficiency,

ρ = terrain reflectivity per steradian,

R = distance from sensor to terrain, and

C_{PI} = path-integrated concentration.

S2 – LiDAR receiver noise equivalent power

The photodetector NEP can be derived by computing the signal (i_s) and noise photocurrent (i_n) using the photodetector responsivity, the LiDAR equations, and the equations for photodetection noise processes. The second harmonic signal photocurrent (RMS) for the gas concentration measurement is given by:

$$i_s = \frac{1}{\sqrt{2}} s P_{DC} \frac{2C_{PI}}{\gamma},$$

where s is the photodetector responsivity. The photodetector noise for a measurement duration Δt is given by:

$$i_n = \sqrt{\left[s^2(RIN)P_{DC}^2 + 2e(sP_{DC} + sP_{amb} + i_{dark}) + \frac{4k_BT}{R_p}\right]\frac{1}{2\Delta t}} = \frac{sNEP}{\sqrt{2\Delta t}},$$

where:

s = photodetector responsivity,

RIN = relative intensity noise on the transmitted LiDAR beam,

e = electron charge,

P_{amb} = ambient light power illuminating photodetector,

i_{dark} = photodetector dark current,

k_B = Boltzmann constant,

T = photodetector temperature, and

R_p = photodetector parallel resistance.

The photodetector noise is defined as a unity signal-to-noise (SNR), such that:

$$\frac{i_s}{i_n} = 1 = \frac{2P_{DC}C_{PI}\sqrt{\Delta t}}{\gamma NEP}.$$

The path-integrated concentration detection limit due to photodetector noise is then given by:

$$C_{PI} = n_{in} = \frac{\gamma NEP}{2P_{DC}\sqrt{\Delta t}} = \frac{\gamma m NEP}{2P_{1f}\sqrt{\Delta t}}.$$

S3 – Gas concentration noise model calibration

The gas concentration noise model parameters for a GML sensor are determined by fitting the model to flight test data, as shown in Figure 6. Given a candidate set of GCN model parameters (detector NEP and speckle noise), the GCN value is computed for each LiDAR measurement using equation 2. The LiDAR gas concentration measurements are then binned by GCN and the standard deviation of gas concentration measurements in each bin is computed to represent the measured gas concentration noise. A least squares optimizer is applied to the modeled and measured GCN values to determine the set of noise parameters (NEP and n_{ci}) that minimizes the squared error between the model and the measurement.

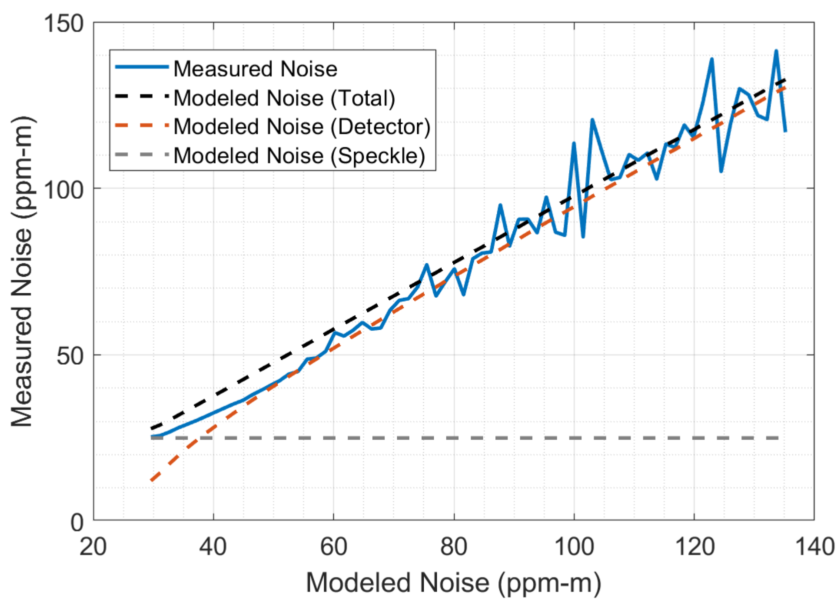

Figure 6. Example fit of noise model to determine the gas concentration noise model parameters for a GML 2.0 sensor from flight test data.

S4 – Raster gas concentration noise computation

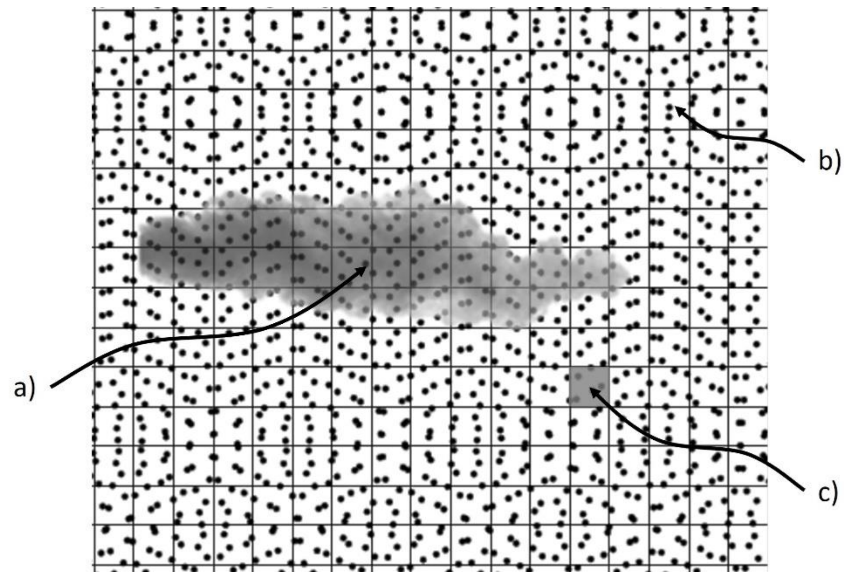

Figure 7. Example of a gas plume a) scanned with GML LiDAR measurements b), which are interpolated onto a regular grid of pixels c).

An example of the spatial distribution of LiDAR points and raster grid are shown in Figure 7. The raster image path-integrated gas concentration pixel values are computed by a weighted average of the individual LiDAR path-integrated gas concentration values within each pixel, where the weighting factors for the individual path-integrated gas concentration LiDAR measurements are derived from the GCN values. Specifically, the pixel path-integrated gas concentration and GCN values are computed using the following equations:

$$c_j = \frac{\sum w_i c_i}{\sum w_i},$$

$$w_i = \frac{1}{GCN_i^2},$$

$$n_j = \frac{1}{\sqrt{\sum w_i}}.$$

where:

j = the j^{th} pixel in the raster grid,

i = the i^{th} LiDAR point in the j^{th} raster pixel,

c_i = the P-Concentration for the i^{th} LiDAR point in the j^{th} raster pixel,

c_j = the weighted average P-Concentration for the j^{th} raster pixel,

w_i = the weighting factor for the i^{th} LiDAR point in the j^{th} raster pixel, and

n_j = the weighted average *GCN* for the j^{th} raster pixel.

S5 – Optimized probability of detection models

Candidate predictor and inverse link functions are shown in Table 2. The pair of predictor and inverse link functions that best represent the controlled release detection data is determined during the PoD model optimization process. Optimized PoD models for both GML sensor versions and each controlled release test region are shown in Table ***3***. The combined GML 2.0 PoD model represents the combination of GML 2.0 controlled release test data sets from all controlled release test regions. The functional form for each PoD Model as a function of emission rate Q, wind speed u, and n = (raster pixel GCN)/1000 is presented. The inverse PoD

Table 2. List of candidate predictor functions and inverse link functions tested for the statistical analysis.

Predictor Functions	Inverse Link Functions
P1: $g(x;\beta) = \dfrac{\beta_1(Q+\beta_5)^{\beta_2}}{n^{\beta_3}u^{\beta_4}}$	Log Normal: $F(g;\alpha) = \dfrac{1}{2}\left[1 + erf\left(\dfrac{ln(g)-\alpha_1}{\sqrt{2}\alpha_2}\right)\right]$
P2: $g(x;\beta) = \dfrac{\beta_1 Q^{\beta_2}}{(n)^{\beta_3}(u+\beta_5)^{\beta_4}}$	Log Logistic: $F(g;\alpha) = \dfrac{1}{1+\left(g/\alpha_1\right)^{-\alpha_2}}$
P3: $g(x;\beta) = \dfrac{\beta_1 Q^{\beta_2}}{(n+\beta_5)^{\beta_3}(u)^{\beta_4}}$	Fréchet: $F(g;\alpha) = e^{-\left(g/\alpha_1\right)^{-\alpha_2}}$
P4: $g(x;\beta) = \dfrac{\beta_1 Q^{\beta_2}}{n^{\beta_3}u^{\beta_4}}$	Burr: $F(g;\alpha) = 1-(1+g^{\alpha_1})^{-\alpha_2}$
	Weibull: $F(g;\alpha) = 1-e^{-\left(g/\alpha_1\right)^{\alpha_2}}$

Table 3. Optimized PoD models for the controlled release data sets from each test region and for the combination of all GML 2.0 controlled release data sets.

Location	PoD Model	Inverse PoD Model	Coefficient Values
Midland, TX GML 1.0	$PoD = 0.5 \times \left(1 + \mathrm{erf}\left(\frac{\left(\frac{\beta_1 Q^{\beta_2}}{n^{\beta_3} u^{\beta_4}}\right) - \alpha_1}{\sqrt{2}\alpha_2}\right)\right)$	$Q = \left(\frac{n^{\beta_3} u^{\beta_4}}{\beta_1} \exp(\sqrt{2}\alpha_2 \times \mathrm{erfinv}(2\mathrm{PoD} - 1) + \alpha_1)\right)^{\frac{1}{\beta_2}}$	α_1 = -0.3466 α_2 = 0.8326 β_1 = 2.998e-4 β_2 = 2.6339 β_3 = 2.7501 β_4 = 2.0877
Los Angeles, CA GML 2.0	$PoD = 1 - \left(1 + \left(\frac{\beta_1 Q^{\beta_2}}{n^{\beta_3}(u + \beta_5)^{\beta_4}}\right)^{\alpha_1}\right)^{-\alpha_2}$	$Q = \left(\frac{1}{\beta_1}((1 - \mathrm{PoD})^{-\frac{1}{\alpha_2}} - 1)^{\frac{1}{\alpha_1}}\ n^{\beta_3}(u + \beta_5)^{\beta_4}\right)^{\frac{1}{\beta_2}}$	α_1 = 2.0000 α_2 = 1.5000 β_1 = 0.1897 β_2 = 1.7999 β_3 = 1.8917 β_4 = 3.2289 β_5 = -2.3488
Bozeman, MT GML 2.0	$PoD = 1 - e^{-\left(\frac{\beta_1 Q^{\beta_2}}{\alpha_1 n^{\beta_3} u^{\beta_4}}\right)^{-\alpha_2}}$	$Q = \left(\frac{\alpha_1}{\beta_1}(-\ln(1 - \mathrm{PoD}))^{\frac{1}{\alpha_2}}\ n^{\beta_3} u^{\beta_4}\right)^{\frac{1}{\beta_2}}$	α_1 = 1.0000 α_2 = 1.0000 β_1 = 33.66e-5 β_2 = 3.1874 β_3 = 3.5578 β_4 = 2.5257
Wonowon, BC GML 2.0	$PoD = 0.5 \times \left(1 + \mathrm{erf}\left(\frac{\left(\frac{\beta_1 Q^{\beta_2}}{n^{\beta_3} u^{\beta_4}}\right) - \alpha_1}{\sqrt{2}\alpha_2}\right)\right)$	$Q = \left(\frac{n^{\beta_3} u^{\beta_4}}{\beta_1} \exp(\sqrt{2}\alpha_2 \times \mathrm{erfinv}(2\mathrm{PoD} - 1) + \alpha_1)\right)^{\frac{1}{\beta_2}}$	α_1 = -0.3466 α_2 = 0.8326 β_1 = 0.0201 β_2 = 2.4088 β_3 = 1.5777 β_4 = 1.9428
Combined GML 2.0	$PoD = 1 - \left(1 + \left(\frac{\beta_1 Q^{\beta_2}}{n^{\beta_3} u^{\beta_4}}\right)^{\alpha_1}\right)^{-\alpha_2}$	$Q = \left(\frac{1}{\beta_1}((1 - \mathrm{PoD})^{-\frac{1}{\alpha_2}} - 1)^{\frac{1}{\alpha_1}}\ n^{\beta_3} u^{\beta_4}\right)^{\frac{1}{\beta_2}}$	α_1 = 2.0000 α_2 = 1.5000 β_1 = 2.41e-3 β_2 = 1.9505 β_3 = 2.0836 β_4 = 1.5185

model represents the emission rate detection threshold as a function of probability of detection *PoD*, wind speed *u*, and *n* = (raster pixel GCN)/1000.

Optimized PoD model selection is performed by minimizing the negative log likelihood function (NLLF) for each combination of candidate predictor and inverse link functions. The optimized NLLF is used to compute the Akaike Information Criterion (AIC) for each candidate pair, and the AIC is used to compute the relative likelihood of minimizing information loss (RLMIL). The function used to compute this value is as follows:

$$RLMIL = \exp\left(\frac{AIC_{min} - AIC_i}{2}\right),$$

where AIC_{min} is the minimum AIC value and AIC_i is the AIC value for the ith unique candidate-predictor combination.[22] The candidate pair with RLMIL equal to one represents the optimal model and is highlighted in green in

Table ***4*** for each data set. The RLMIL for non-optimal models represents the probability that it is the model that best represents the data.

Table 4. Relative likelihood of minimizing information (RLMIL) for candidate PoD models. Optimal PoD model (i.e. combination of predictor and inverse link functions) has RLMIL equal to one and is highlighted in green. The second-best performing model is highlighted in yellow, and the best performing predictor function is highlighted in blue.

Predictor Function	Inverse Link Function	Midland GML 1.0	Los Angeles GML 2.0	Bozeman GML 2.0	British Columbia GML 2.0	Combined GML 2.0
p1	Log Normal	0.3609	0.6385	0.1259	0.3613	0.3534
p1	Log Logistic	0.1497	0.5803	0.0320	0.2696	0.1271
p1	Fréchet	0.0042	0.0342	0.0003	0.0473	0.0000
p1	Burr	0.3113	0.8049	0.1009	0.3422	0.3655
p1	Weibull	0.3131	0.8088	0.3744	0.2457	0.0462
p2	Log Normal	0.5979	0.7621	0.1262	0.5691	0.4094
p2	Log Logistic	0.2698	0.8557	0.0326	0.3937	0.1434
p2	Fréchet	0.0055	0.0473	0.0003	0.0688	0.0000
p2	Burr	0.5930	1.0000	0.1061	0.5260	0.4287
p2	Weibull	0.5191	0.4324	0.4633	0.4334	0.0450
p3	Log Normal	0.6040	0.7596	0.1440	0.4015	0.6062
p3	Log Logistic	0.2820	0.7496	0.0369	0.2876	0.1739
p3	Fréchet	0.0124	0.0542	0.0003	0.0477	0.0000
p3	Burr	0.5266	0.9512	0.1202	0.3783	0.5477
p3	Weibull	0.3321	0.5515	0.5021	0.2900	0.0728
p4	Log Normal	1.0000	0.6621	0.3389	1.000	0.9663
p4	Log Logistic	0.4055	0.6630	0.0878	0.7347	0.3411
p4	Fréchet	0.0117	0.0482	0.0009	0.1234	0.0000
p4	Burr	0.8500	0.7910	0.2749	0.9459	1.0000
p4	Weibull	0.8408	0.4407	1.0000	0.6574	0.0874

The p4 predictor function is found to best represent the controlled release data in three of the four region-specific data sets and the combined GML 2.0 data set, while the p2 model is found to be optimal for the LA data set. Predictors functions p1-p3 are less likely to minimize information loss because small reductions in the NLLF observed when fitting PoD models to the controlled release data are outweighed by the penalty for including an additional model parameter. Depending on the data set the Log Normal, Burr, and Weibull inverse link functions are found to be optimal, whereas the Log Logistic and Fréchet inverse link functions are less competitive.

A comparison of the optimized GML 2.0 PoD models for each data set is shown in Figure 8. The black lines in Figure 8 a) & b) show the optimal PoD model for the combined data set at three PoD levels and

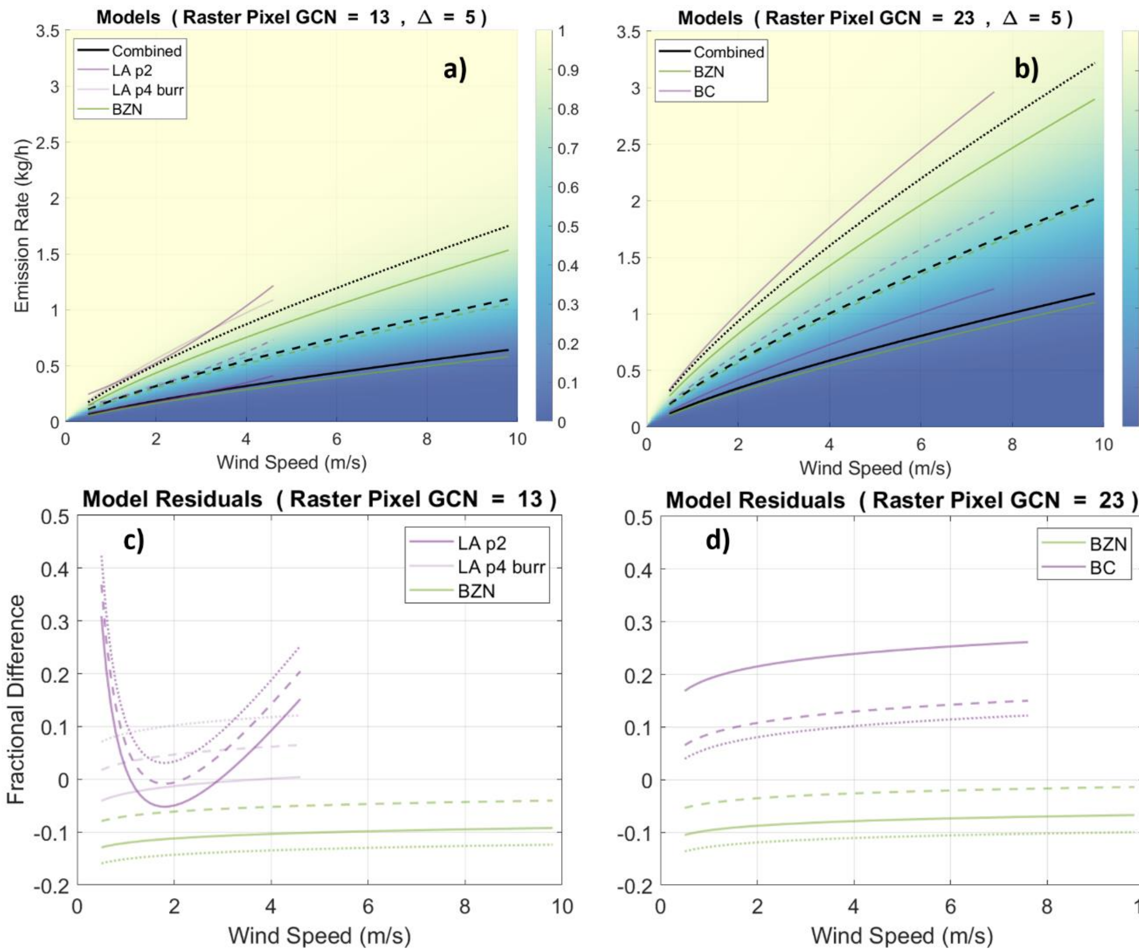

Figure 8. a) & b) Comparison of optimized PoD models for individual data sets with combined model at 10% (solid), 50% (dashed), and 90% (dotted) PoD for 13 ppm-m and 23 ppm-m raster pixel GCN values, respectively. c) & d) Residual plots showing fractional differences between optimized PoD model for individual data sets compared to the combined PoD model for 13 ppm-m and 23 ppm-m raster pixel GCN values, respectively.

two raster pixel GCN levels. The purple and green lines show the optimal PoD models for the individual LA, BZN, and BC data sets, respectively. Figure 8 c) & d) show the fractional differences between the individual data set models and the combined model. Individual models typically agree with the combined model to within 20% fractional difference across most of the valid wind speed range and at both raster pixel GCN values.

S6 – Aggregate controlled release data sets

The aggregate controlled release data set for all valid GML 2.0 flyover passes described in Table 1 is shown in Figure 9. The aggregate controlled release data set for all valid GML 1.0 flyover passes can be found in Ref. [7].

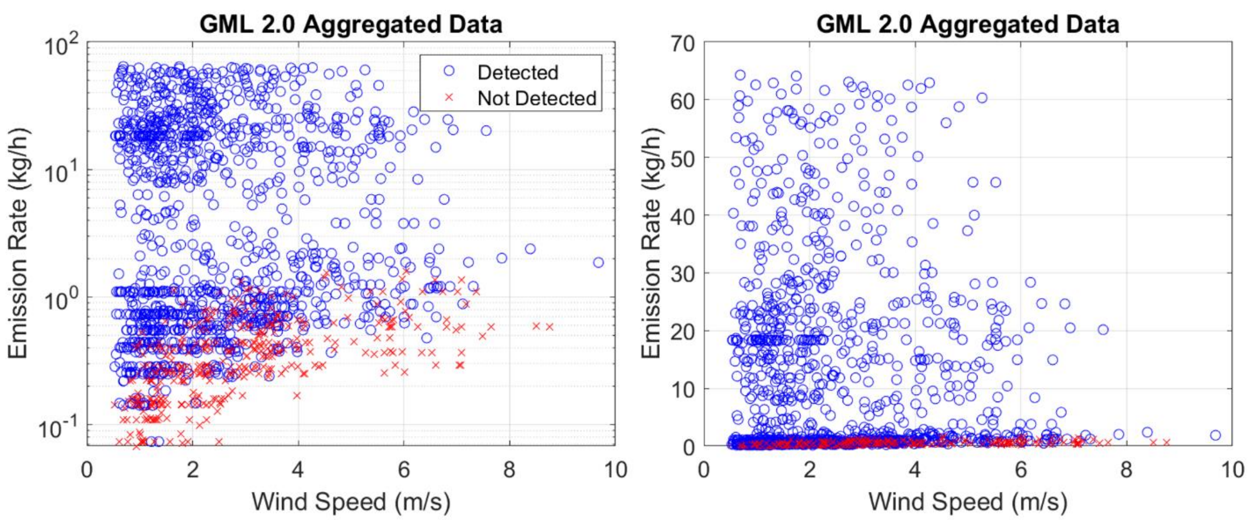

Figure 9. Semi-log plot of emission rate versus wind speed for all valid GML 2.0 flyover passes (left). Linear plot of emission rate versus wind speed for all valid GML 2.0 flyover passes (right).

References

[1] Shindell, D. et al. Global Methane Assessment: Benefits and Cost of Mitigating Methane Emissions. *United Nations Environment Programme* **2021**

[2] Global Methane Tracker 2023. *International Energy Agency* **2023**

[3] Peischl, J.; Eilerman, S. J.; Neuman, J. A.; Aikin, K. C.; De Gouw, J.; Gilman, J. B.; Herndon, S. C.; Nadkarni, R.; Trainer, M.; Warneke, C.; Ryerson, T. B. Quantifying Methane and Ethane Emissions to the Atmosphere From Central and Western U.S. Oil and Natural Gas Production Regions. JGR Atmospheres **2018**, 123 (14), 7725–7740. https://doi.org/10.1029/2018JD028622.

[4] Johnson, M.R.; Tyner, D.R. Tyner; Conley, Schwitzke, S.; Zavala-Araiza, D. Comparisons of Airborne Measurements and Inventory Estimates of Methane Emissions in the Alberta Upstream Oil and Gas Sector, *Environmental Science & Technology,* **2017** 51 (21) 13008-13017. https://doi.org/10.1021/acs.est.7b03525

[5] Barkley, Z.; Davis, K.; Miles, N.; Richardson, S.; Deng, A.; Hmiel, B.; Lyon, D.; Lauvaux, T. Quantification of Oil and Gas Methane Emissions in the Delaware and Marcellus Basins Using a Network of Continuous Tower-Based Measurements. Atmos. Chem. Phys. **2023**, 23 (11), 6127–6144. https://doi.org/10.5194/acp-23-6127-2023.

[6] Jacob, D. J.; Varon, D. J.; Cusworth, D. H.; Dennison, P. E.; Frankenberg, C.; Gautam, R.; Guanter, L.; Kelley, J.; McKeever, J.; Ott, L. E.; Poulter, B.; Qu, Z.; Thorpe, A. K.; Worden, J. R.; Duren, R. M. Quantifying Methane Emissions

from the Global Scale down to Point Sources Using Satellite Observations of Atmospheric Methane. Atmos. Chem. Phys. **2022**, 22 (14), 9617–9646. https://doi.org/10.5194/acp-22-9617-2022.
[7] Bell, C.; Rutherford, J.; Brandt, A.; Sherwin, E.; Vaughn, T.; Zimmerle, D. Single-blind determination of methane detection limits and quantification accuracy using aircraft-based LiDAR. *Elementa* **2022** 10 00080. https://doi.org/10.1525/elementa.2022.00080
[8] Conrad, B. M.; Tyner, D. R.; Johnson M. R. Robust probabilities of detection and quantification uncertainty for aerial methane detection; Examples for three airborne technologies. *Remote Sens. Environ.* **2023**, 288, 113499. https://doi.org/10.1016/j.rse.2023.113499
[9] Johnson, M.; Conrad, B. M.; Tyner, D. R. Creating measurement-based oil and gas sector methane inventories using source-resolved aerial surveys. *Commun. Earth Environ.* **2023**, 4, 139. https://doi.org/10.1038/s43247-023-00769-7
[10] Conrad, B.M.; Tyner, D.R.; Li, H.Z.; Donglai, X.; Johnson M.R. A measurement-based upstream oil and gas methane inventory for Alberta, Canada reveals higher emissions and different sources than official estimates. *Commun. Earth Environ.* **2023** 4 416. https://doi.org/10.1038/s43247-023-01081-0
[11] Ravikumar, A.P.; Tullos E.E.; Allen, D.T.; Cahill, B.; Hamburg, S.P.; Zimmerle, D.; Fox, T.A.; Caltagirone, M.; Owens, L.; Stout, R.; Grimes, A.J.; Fernandez, T.M.; Jenks, C.; Duren, R.; Halff, A.; Bazilian, M.D.; Rucker, S. Measurement-based differentiation of low-emission global natural gas supply chains Nature Energy **2023**, 8, 1147-1176. https://doi.org/10.1038/s41560-023-01381-x
[12] Sherwin, E. D.; Chen, Y.; Ravikumar, A. P.; Brandt A. R. Single-blind test of airplane-based hyperspectral methane detection via controlled releases *Science of the Anthropocene* **2021**; 9, 1. https://doi.org/10.1525/elementa.2021.00063
[13] Kunkel W. M.; Carre-Burritt, Aivazian, G. S.; Snow, N. C.; Harris, J. T.; Mueller, T. S.; Roos, P. A.; Thorpe, M. J Extension of Methane Emission Rate Distribution for Permian Basin Oil and Gas Production Infrastructure by Aerial LiDAR. *Environ. Sci. Technol.* **2023**, 57, 33, 12234-12241. https://doi.org/10.1021/acs.est.3c00229
[14] Cusworth, D. H.; Duren, R. M.; Thorpe, A. K.; Olsen-Duvall, W.; Heckler, J.; Chapman, J. W.; Eastwood, M. L.; Helmlinger, M. C.; Green, R. O.; Asner, G. P.; Dennison, P. E.; Miller, C. E. Intermittency of Large Methane Emitters in the Permian Basin. *Environ. Sci. Technol. Lett.* **2021**, 8, 567-573. https://doi.org/10.1021/acs.estlett.1c00173
[15] El Abbadi, S. H.; Chen, Z.; Burdeau, P. M.; Rutherford, J. S.; Chen, Y.; Zhang, Z.; Sherwin, E. D.; Brandt, A. R. Comprehensive evaluation of aircraft-based methane sensing for greenhouse gas mitigation, preprint, **2023**. https://doi.org/10.31223/X51D4C.
[16] Johnson, M. R.; Tyner, D. R.; Szekeres, A. J. Blinded evaluation of airborne methane source detection using Bridger Photonics LiDAR. *Remote Sens. Environ.* **2021** 259, 112418. https://doi.org/10.1016/j.rse.2021.112418
[17] Thorpe, M. J.; Kreitinger, A. T. APPARATUSES AND METHODS FOR GAS FLUX MEASUREMENTS. US-2021/0055180 **2021**
[18] Kreitinger, A. T.; Thorpe, M. J. APPARATUSES AND METHODS FOR ANOMALOUS GAS CONCENTRATION DETECTION. WO-US-01 11112308 **2021**
[19] Iseki T.; Tai, H.; Kimura, K., A Compact Remote Methane Sensor using a Tunable Diode Laser, *Meas. Sci.Technol*., **2000** 11, 594. https://doi.org/10.1088/0957-0233/11/6/302
[20] Sheen, David M. *Frequency Modulation Spectroscopy Modeling for Remote Chemical Detection*. United States. **2000**. https://doi.org/10.2172/1023146
[21] Masiyano, D., et. al. Use of diffuse reflections in tunable diode laser absorption spectroscopy: implications of laser speckle for gas absorption measurements. *Appl. Phys. B*, **2008**, 90, 279-288. https://doi.org/10.1007/s00340-007-2896-z
[22] Burnham, K. P.; Anderson, D. R. Model Selection and Multimodel Inference: A practical information-theoretic approach. Springer New York: New York, NY, **2002**.